IJMMM International Journal of Minerals, Metallurgy and Materials 矿物冶金与材料学报（英文版）

Electrochemical extraction of strontium from molten salts using reactive zinc and aluminum electrodes

Yongcheng Zhang, Taiqi Yin, Lei Zhang, Xiaochen Zhang, Tao Bo, Xiaoli Tan, Mei Li, and Wei Han

Cite this article as:
Yongcheng Zhang, Taiqi Yin, Lei Zhang, Xiaochen Zhang, Tao Bo, Xiaoli Tan, Mei Li, and Wei Han, Electrochemical extraction of strontium from molten salts using reactive zinc and aluminum electrodes, *Int. J. Miner. Metall. Mater.*, 32(2025), No. 4, pp. 892-901. https://doi.org/10.1007/s12613-024-2939-z

View the article online at SpringerLink or IJMMM Webpage.

Articles you may be interested in

Zhen Zhang, Pan Luo, Yan Zhang, Yuhan Wang, Li Liao, Bo Yu, Mingshan Wang, Junchen Chen, Bingshu Guo, and Xing Li, Effects of conductive agent type on lithium extraction from salt lake brine with $LiFePO_4$ electrodes, *Int. J. Miner. Metall. Mater.*, 31(2024), No. 4, pp. 678-687. https://doi.org/10.1007/s12613-023-2750-2

IJMMM WeChat

QQ author group

INTERNATIONAL JOURNAL OF
Minerals, Metallurgy and Materials

Volume 32, Number 4, April 2025
Page 892

Research Article https://doi.org/10.1007/s12613-024-2939-z

Electrochemical extraction of strontium from molten salts using reactive zinc and aluminum electrodes

Yongcheng Zhang[1,2,4),*], *Taiqi Yin*[1,4),*,✉], *Lei Zhang*[1,4)], *Xiaochen Zhang*[1,4)], *Tao Bo*[1,4)], *Xiaoli Tan*[3)], *Mei Li*[2),✉], *and Wei Han*[2)]

1) Zhejiang Key Laboratory of Data-Driven High-Safety Energy Materials and Applications, Ningbo Institute of Materials Technology and Engineering, Chinese Academy of Sciences, Ningbo 315201, China

2) College of Materials Science and Chemical Engineering, Harbin Engineering University, Harbin 150001, China

3) MOE Key Laboratory of Resources and Environmental System Optimization, College of Environmental Science and Engineering, North China Electric Power University, Beijing 102206, China

4) Qianwan Institute of CNITECH, Ningbo 315336, China

(Received: 11 March 2024; revised: 20 May 2024; accepted: 21 May 2024)

Abstract: Herein, the electrochemical behaviors of Sr on inert W electrode and reactive Zn/Al electrodes were systematically investigated in LiCl–KCl–$SrCl_2$ molten salts at 773 K using various electrochemical methods. The chemical reaction potentials of Li and Sr on reactive Zn/Al electrodes were determined. We observed that Sr could be extracted by decreasing the activity of the deposited metal Sr on the reactive electrode, although the standard reduction potential of Sr(II)/Sr was more negative than that of Li(I)/Li. The electrochemical extraction products of Sr on reactive Zn and Al electrodes were $Zn_{13}Sr$ and Al_4Sr, respectively, with no codeposition of Li observed. Based on the density functional theory calculations, both $Zn_{13}Sr$ and Al_4Sr were identified as stable intermetallic compounds with Zn-/Al-rich phases. In LiCl–KCl molten salt containing 3wt% $SrCl_2$, the coulombic efficiency of Sr in the Zn electrode was ~54%. The depolarization values for Sr on Zn and Al electrodes were 0.864 and 0.485 V, respectively, exhibiting a stronger chemical interaction between Zn and Sr than between Al and Sr. This study suggests that using reactive electrodes can facilitate extraction of Sr accumulated while electrorefining molten salts, thereby enabling the purification and reuse of the salt and decreasing the volume of the nuclear waste.

Keywords: strontium; reductive extraction; molten salt; depolarization effect; reactive electrode

1. Introduction

Nuclear energy represents a long-term source of energy to meet the demands of developed countries [1]. Advanced nuclear energy systems generate substantial quantities of spent nuclear fuel, which requires management via open or closed fuel cycles. Closed fuel cycles can considerably enhance the utilization efficiency of nuclear fuel but necessitate separation of the fission products [2].

Spent nuclear fuel comprises fission products, actinides, and unreacted uranium. Of the hundreds of fission product isotopes generated, most rapidly decay into nonradioactive isotopes. A notably important exception is ^{90}Sr, one of the fission products posing considerable concern. The radiotoxicity of ^{90}Sr, with a half-life of ~29 years, decays via the emission of highly energetic gamma rays. It represents a considerable proportion of the radioactivity in nuclear waste fission products, requiring ~300 years to diminish to the levels of natural uranium ore. Consequently, the separation of Sr from nuclear waste can substantially increase the spatial utilization efficiency of geological repository [3]. Meanwhile, pyroprocessing is currently one of the most promising technologies for treating commercially spent nuclear fuel and reducing the capacity required in nuclear waste storage facilities [4]. Electrorefining of metallic fuels is a key unit operation in pyroprocessing. As the electrorefining process proceeds, $SrCl_2$ gradually accumulates in the molten salt, affecting the properties of the molten salt and thereby influencing the separation of lanthanides and actinides. Research on the separation and extraction of Sr has also contributed to the purification and reuse of molten salts in the electrorefining process [5].

Purification of molten salts following electrorefining enables the reuse of these salts, necessitating the extraction of accumulated fission products in the molten salt [6]. Fission products in the molten salts include rare earth elements, alkali metals, and alkaline earth metals. Selective separation of these elements can facilitate segregated storage, considerably reducing the volume of waste [7]. Accordingly, researchers have developed various methods, such as ion ex-

*These authors contributed equally to this work.

✉ Corresponding authors: Taiqi Yin E-mail: yintaiqi@nimte.ac.cn; Mei Li E-mail: meili@hrbeu.edu.cn

© University of Science and Technology Beijing 2025

Springer

change [8–9], precipitation [10–13], and melt crystallization [14–16]. However, the efficiency of removing fission products via precipitation was relatively low. While ion exchange offers higher efficiency, it generates a considerable amount of ceramic waste and incurs higher costs. Melt crystallization provides higher efficacy in immobilizing Sr, although it requires further development for practical application. Using electrochemical methods to extract Sr from waste salts following electrorefining can simplify the process flow and reduce costs.

Matsumiya *et al*. [17] researched the extraction of Sr using various electrodes, including Al, Bi, Pb, Sn, and Zn electrodes in KCl–$SrCl_2$ and KCl–NaCl–$SrCl_2$ molten salts. The results indicated that Sr could be extracted only in the KCl–$SrCl_2$ molten salt using Al and Pb electrodes. This indicates the following: 1) Al and Pb exhibit strong chemical interactions with Sr, and 2) Na has a considerable thermodynamic influence on Sr extraction [18–19]. S.W. Kim *et al*. [20] investigated the extraction of Ba and Sr using Ni electrodes in LiCl–$BaCl_2$–$SrCl_2$ molten salt. The results indicated that the amount of Ba and Sr in the deposits was almost negligible compared with that of Li. H. Kim and co-workers [21–23] researched the extraction of Sr and Ba using various reactive electrodes in LiCl–KCl–$BaCl_2$–$SrCl_2$ molten salt. The results demonstrated that the effectiveness of Bi and Sb was superior to that of Sn and Pb. Further investigations with Bi–Sb alloy electrodes revealed an improvement in extraction efficiency for Ba, while the efficiency for Sr decreased. In addition, the codeposition of Li was observed in these cases. However, Woodes and Phongikaroon [24] evaluated the recovery of Cs, Sr, and Ba in LiCl–KCl salt using a liquid Bi electrode, and the findings indicated that the extraction of Cs, Sr, and Ba was not thermodynamically favorable. Jang *et al*. [25] studied the extraction of Sr(II) and Cs(I) using various reactive electrodes in LiCl–KCl molten salt. The results demonstrated that the Sr extraction efficiency on Zn electrodes was superior to that on Bi, Cd, and Pb electrodes; however, Cs was almost nonextractable.

Table 1 presents the standard reduction potentials of pure chlorides calculated on the basis of standard free energy at 773 K [26]. $SrCl_2$ is thermodynamically more stable than LiCl; therefore, it cannot be separated from the electrolyte via electrochemical deposition on an inert cathode. However, Sr extraction and separation can be feasibly achieved by shifting the deposition potential to a more positive value by decreasing the activity of the deposited metal Sr on the reactive electrode. Moreover, research on the electrochemical behavior of Sr in molten salt systems has been limited, and comparative experiments involving various electrodes have been scarce, with some experimental results showing discrepancies. Therefore, as the research topic, we selected two metals that exhibit considerable depolarization effects of Sr on reactive electrodes. The main focus is to explore the feasibility of separating Sr in LiCl–KCl, followed by examining the depolarization effects of Sr on reactive electrodes, as well as examining the compounds formed after extraction.

Table 1. Standard reduction potentials (E^0) of pure chlorides calculated using the standard free energy at 773 K

Redox couple	E^0 / V vs. Cl^-/Cl_2
KCl/K	−3.759
$SrCl_2$/Sr	−3.689
LiCl/Li	−3.574
$AlCl_3$/Al	−1.866
$ZnCl_2$/Zn	−1.573

2. Experimental

2.1. Electrochemical cell components and assembly

Anhydrous lithium chloride (>99.0%) and potassium chloride (>99.9%) were purchased from Xilong Chemical Co., Ltd. Anhydrous aluminum chloride (>99.9%) and $ZnCl_2$ (>99.9%) were purchased from Sinopharm Chemical Reagent Co., Ltd. $SrCl_2$ (>99.9%) and Zn grains (>99.9%) were purchased from Shanghai Aladdin Biochemical Technology Co., Ltd. The Ag wire (ϕ1 mm, >99.99%), W wire (ϕ1 mm, >99.99%), and Al wire (ϕ1 mm, >99.99%) were purchased from Beijing Hengyuan Zhuoli Technology Development Co., Ltd.

The LiCl–KCl was weighed as per the eutectic salt ratio (LiCl : KCl = 59:41, mol%) and then placed in a vacuum oven at 423 K for 24 h to remove residual moisture. Subsequently, it was transferred into a muffle furnace within a glove box and heated to 773 K to melt. The electrochemical behavior was investigated using a three-electrode system. The working electrodes included both inert and reactive electrodes. The inert electrode was a tungsten wire with a 1 mm diameter and 20 cm length. The reactive electrodes were an aluminum wire with a 1-mm diameter and 20-cm length and zinc granules. The zinc granules were placed in an alumina crucible and connected using a molybdenum wire with a 0.5-mm diameter and 20-cm length as the conductor. The counter electrode was a graphite rod in spectral purity with a 4-mm diameter and 20-cm length. The reference electrode was prepared by uniformly mixing 1wt% AgCl into the LiCl–KCl eutectic salt and then loading it into an alumina crucible using a Ag wire as the conductor.

2.2. Electrochemical techniques

All electrochemical experiments were conducted in a glove box (Vigor) under an argon atmosphere with the water and oxygen contents maintained below 1 ppm. All electrochemical measurements were conducted using an AutoLab PGSTAT 302N potentiostat/galvanostat. Cyclic voltammetry (CV), square wave voltammetry (SWV), and chronopotentiometry (CP) were employed to identify the signals of intermetallic compounds between Zn–Sr and Al–Sr, thereby determining the depolarization effects. Open circuit chronopotentiometry (OCP) was used to analyze chemical reactions occurring at various potentials. Constant current electrolysis and the galvanostatic intermittent titration technique (GITT) were used for Sr extraction.

2.3. Preparation and characterization of cathodic deposits

The products obtained post-electrolysis were removed from the molten salt and treated with ultrapure water and alcohol to remove any salt residues from their surface. X-ray diffraction (XRD) (Bruker, D8 Advance) was used for analysis of the alloy compositions. Scanning electron microscopy (SEM) (ZEISS GeminiSEM 300) equipped with energy-dispersive spectrometry (EDS) (Bruker XFlash 6I100) was employed to analyze the microstructure.

2.4. Density functional theory calculations

The formation energies were calculated using the projector augmented-wave method [27] based on the density functional theory (DFT) as implemented in the Vienna Ab Initio Simulation Package [28]. The exchange correlation functional was described using the Perdew–Burke–Ernzerhof generalized gradient approximation method. The plane-wave cutoff energy was set to 600 eV, and Gaussian smearing with a smearing value of 0.1 eV was used. Brillouin zone integration was calculated using sufficiently dense Monkhorst–Pack *k*-point meshes to ensure that the energy calculations satisfactorily converged within 1 meV per atom. All the geometries were relaxed until all forces on the atoms were smaller than 0.003 eV·Å^{-1}. The formation energy was calculated as follows:

$$\Delta E_f = E_{tot} - \sum_i \mu_i x_i \quad (1)$$

where E_{tot} represents the DFT total energy of the compound, μ_i is DFT total energy per atom for the bulk Al/Zn metal, and x_i is quantity of the compound.

3. Results and discussion

3.1. Electrochemical coreduction of Sr(II) and Zn(II)

We used CV to investigate the codeposition behavior of Sr(II) and Zn(II) on a W electrode in LiCl–KCl molten salt, and the results are shown in Fig. 1. Fig. 1(a) shows the CV curves obtained after adding $ZnCl_2$ (1wt%) to the blank LiCl–KCl salt, where A/A' represents the reduction and oxidation signals of Li and a pair of peaks B/B' at −0.79/−0.58 V corresponds to the oxidation/reduction signals of Zn. Between the A/A' and B/B' signals, two pairs of redox signals, C/C' and D/D', correspond to two types of Zn–Li alloys [29]. Upon addition of $SrCl_2$ to the LiCl–KCl–$ZnCl_2$ system, a new pair of oxidation/reduction peaks, E/E', appeared at −1.83/−1.71 V, attributed to the formation of the Zn–Sr intermetallic compound. The electrode potential of the Zn–Sr alloy was more positive than that of Zn–Li, indicating that Sr has a stronger depolarizing effect in Zn than Li. This also suggests the possibility of extracting Sr from Zn. In addition, the formation of C/C' was suppressed because of the emergence of E/E'.

SWV was conducted in LiCl–KCl–$ZnCl_2$ and LiCl–KCl–$ZnCl_2$–$SrCl_2$ molten salts to further confirm the emergence of E/E' and disappearance of C/C', as shown in Fig. 2. By comparing the red and black curves, we observed that the initial reduction potentials of C and E were nearly equal. The formation of E on the electrode surface suppressed the generation of C. The appearance of E did not affect the formation of D because the reduction potential for D occurred at a more negative value.

Fig. 3 shows the OCP curve for LiCl–KCl–$ZnCl_2$ (1wt%)–$SrCl_2$ (3wt%) molten salt. Each plateau corresponds to a different chemical reaction. By comparing with the experimental results obtained from SWV and CV, the plateaus can be attributed to the following reactions:

$$\text{Plateau I}: \ \mathrm{Li(0)} \leftrightarrow \mathrm{Li(I)} + \mathrm{e^-} \quad (2)$$

$$\text{Plateau II}: \ \mathrm{Zn_xLi_y} \leftrightarrow x\mathrm{Zn(II)} + y\mathrm{Li(I)} + (2x+y)\mathrm{e^-} \quad (3)$$

$$\text{Plateau III}: \ \mathrm{Zn_xSr_y} \leftrightarrow x\mathrm{Zn(II)} + y\mathrm{Sr(II)} + (2x+2y)\mathrm{e^-} \quad (4)$$

$$\text{Plateau IV}: \ \mathrm{Zn(0)} \leftrightarrow \mathrm{Zn(II)} + 2\mathrm{e^-} \quad (5)$$

On the basis of the abovementioned discussion, the depolarization value (ΔE) can be expressed [21,30] as follows:

$$\Delta E = E_R - E_W \quad (6)$$

where E_R and E_W correspond to the equilibrium potential of Sr(II) on reactive and inert electrodes, respectively. In this study, E_W corresponds to the equilibrium potential of E

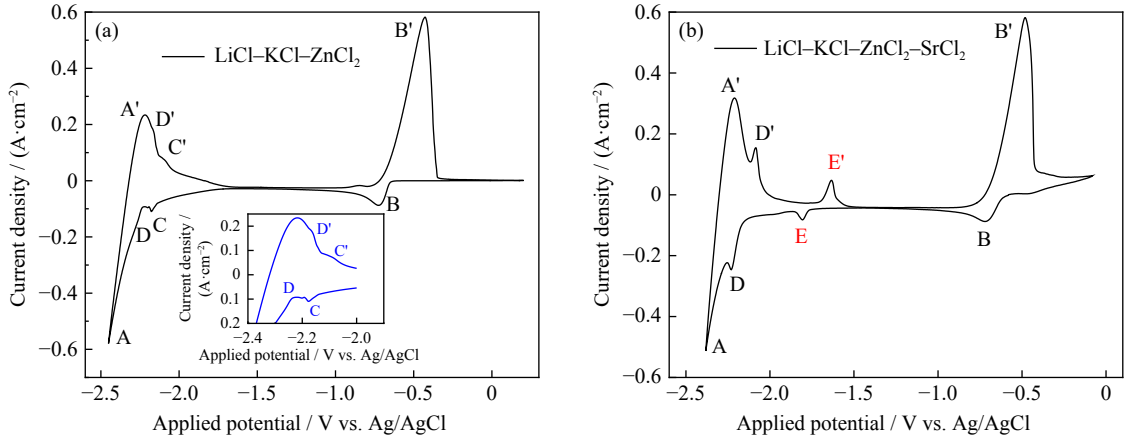

Fig. 1. CV curves recorded for various molten salts on W electrodes at a scanning rate of 0.1 V·s^{-1}: (a) LiCl–KCl–$ZnCl_2$ (1wt%) and (b) LiCl–KCl–$ZnCl_2$ (1wt%)–$SrCl_2$ (3wt%).

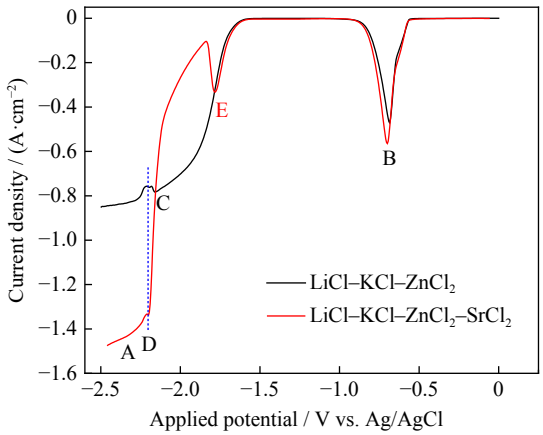

Fig. 2. SWV curves recorded for KCl–LiCl–$ZnCl_2$ (1wt%) and KCl–LiCl–$ZnCl_2$ (1wt%)–$SrCl_2$ (3wt%) on W electrodes under the following conditions: 25 mV pulse height, 1 mV potential step, and 10 Hz frequency.

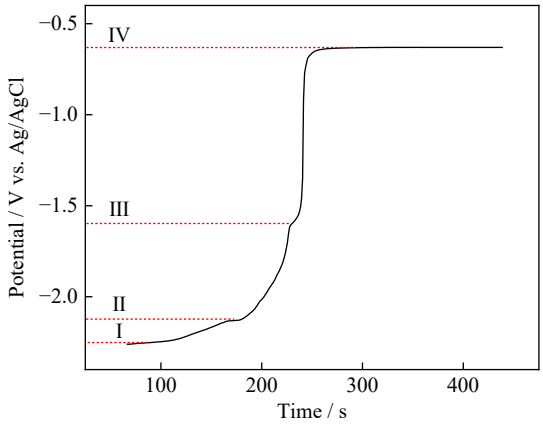

Fig. 3. OCP curve recorded for LiCl–KCl–$ZnCl_2$ (1wt%)–$SrCl_2$ (3wt%) molten salt. Working electrode: W; electrode area: 0.322 cm^2; deposition potential: −2.5 V; deposition time: 60 s.

(Fig. 1(b)). The value of E_R corresponds to the standard potential of Sr(II)/Sr because the reduction potential of Sr is more negative than that of Li. Hence, the depolarization value of Sr on Zn is ~0.864 V.

CP was conducted in LiCl–KCl–$ZnCl_2$ (1wt%)–$SrCl_2$ (3wt%) molten salt at various current intensities at 773 K, as shown in Fig. 4. At an applied current intensity of −11 mA, the first plateau (denoted as plateau 1) appeared at approximately −0.78 V, corresponding to the reduction of Zn. With the increase in applied current intensity to −13 mA, a second plateau emerged at approximately −1.79 V, corresponding to the Zn–Sr alloy. Further increasing the current intensity resulted in the gradual appearance of the third and fourth plateaus, corresponding to Zn–Li alloy and Li metal, respectively. The transition time τ was related to the diffusion of atoms. Fig. 4(b) shows the relationship curve between the current multiplied by the square root of the transition time and the applied current. Fig. 4(b) shows two lines parallel to the *x*-axis, confirming that the diffusion coefficient can be calculated using the Sand equation [31]:

$$I\tau^{1/2} = \frac{nFSC_0(\pi D)^{1/2}}{2} \quad (7)$$

where I represents current, τ is transition time measured in the chronopotentiogram, n is number of transferred electrons, F is the Faraday constant, C_0 is concentration, S is electrode surface area, and D is diffusion coefficient of electroactive species.

The calculated diffusion coefficient of Zn in the molten salt was 1.65×10^{-5} $cm^2 \cdot s^{-1}$, and the diffusion coefficient of Sr in Zn was 6.71×10^{-6} $cm^2 \cdot s^{-1}$.

3.2. Electrochemical reduction of Sr(II) and Al(III)/Al

The codeposition behavior of Sr(II) with Al(III) on a W electrode in LiCl–KCl molten salt was investigated using CV. Fig. 5(a) shows the comparative cyclic voltammograms of the LiCl–KCl–$AlCl_3$ (0.5wt%) and LiCl–KCl–$AlCl_3$ (0.5wt%)–$SrCl_2$ (3wt%) molten salts on the W electrode. The reduction/oxidation signals A2/A2' and B2/B2' correspond to the reduction and oxidation of Li and Al, respectively. A detailed analysis of the localized region is required owing to the Al–Li and Al–Sr alloy signals. By comparing the signals in Fig. 5(b), in which C2/C2' (−2.18/−2.12 V) corresponds to the reduction and oxidation of the Al–Li alloy, the three pairs of reduction/oxidation peaks D2/D2' (−2.31/−2.17 V), E2/E2'

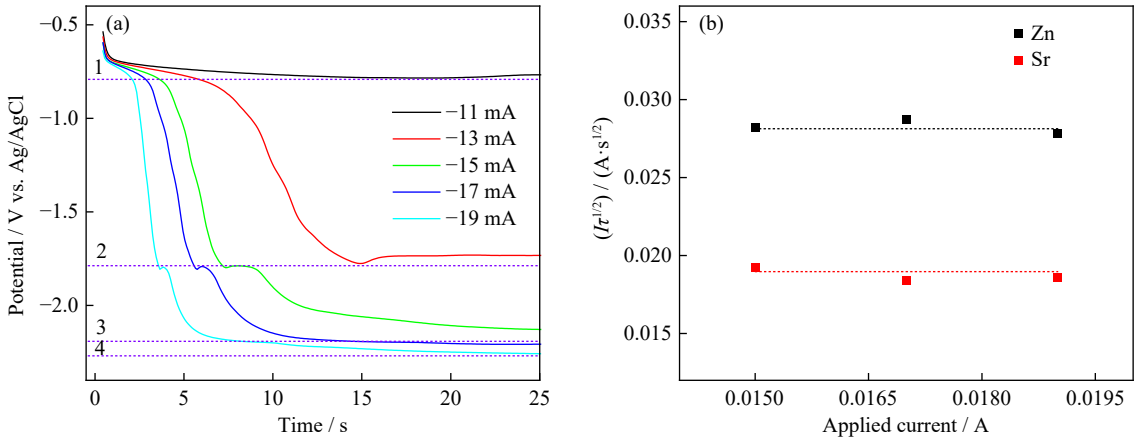

Fig. 4. (a) Chronopotentiograms obtained for molten LiCl–KCl–$ZnCl_2$ (1wt%)–$SrCl_2$ (3wt%) system on the W electrode (S = 0.322 cm^2) at various currents. (b) Relationship curve between the current multiplied by the square root of the transition time and current.

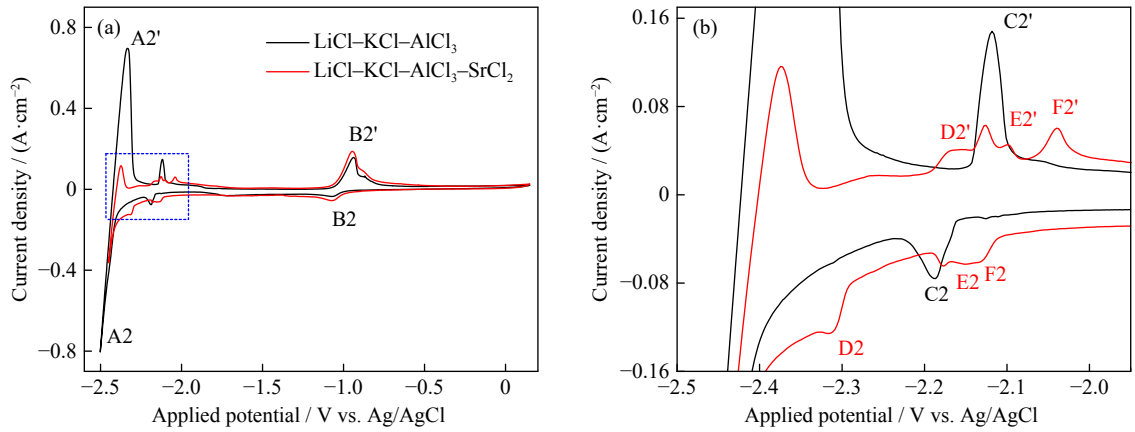

Fig. 5. (a) CV curves obtained for LiCl–KCl–$AlCl_3$ (0.5wt%) (black line) and LiCl–KCl–$AlCl_3$ (0.5wt%)–$SrCl_2$ (3wt%) molten salt (red line) on W electrodes (S = 0.322 cm^2); (b) the corresponding magnified curves.

(−2.15/−2.10 V), and F2/F2' (−2.13/−2.04 V) correspond to three types of Al–Sr intermetallic compounds, respectively. Exactly three intermetallic compounds are present as per the Al–Sr binary alloy phase diagram [32]. Because the electrode potential of Al is more positive than that of Sr, the potential of the Al–Sr intermetallic compounds lies between those of Al and Sr, with the Al-rich phase having a more positive potential than the Sr-rich phase. Therefore, D2/D2', E2/E2', and F2/F2' correspond to Al_7Sr_8, Al_2Sr, and Al_4Sr, respectively. Noteworthily, the potentials corresponding to the two Al–Sr intermetallic compounds represented by E2/E2' and F2/F2' are more positive than that of the Al–Li intermetallic compound represented by C2/C2', indicating that Sr has a stronger depolarizing effect in Al than Li.

SWV was conducted on a W electrode at 773 K in LiCl–KCl–$AlCl_3$ (0.5wt%)–$SrCl_2$ (3wt%) molten salt to further ascertain the reproducibility of the Al–Li and Al–Sr alloy signals (Fig. 6). The magnified section in Fig. 6(b) reveals four reduction peaks corresponding to C2, D2, E2, and F2 in the CV curve.

The discussion of the results from Figs. 5 and 6 shows that Sr has a stronger depolarizing effect in Al than Li, indicating that Sr can be extracted on an Al electrode. To further confirm the feasibility of extracting Sr in Al, we performed the CV analysis of the LiCl–KCl–$SrCl_2$ (3wt%) system on an Al electrode. Fig. 7(a) compares the CV curves of the LiCl–KCl and LiCl–KCl–$SrCl_2$ (3wt%) molten salt systems on an Al electrode. E3/E3' and F3/F3' correspond to signals of two types of Al–Sr intermetallic compounds. Fig. 7(b) shows the SWV curve for LiCl–KCl–$SrCl_2$ (3wt%) on an Al electrode, clearly distinguishing the reduction signals of the two intermetallic compounds, E3 and F3.

An OCP curve was recorded for LiCl–KCl–$SrCl_2$ (3wt%) molten salt following constant potential electrolysis at −2.2 V for 60 s. As seen in Fig. 8, three plateaus appeared, which can be attributed to the following reactions:

$$\text{Plateau I}: \ Al_xLi_y \leftrightarrow xAl + yLi\,(I) + ye^- \tag{8}$$

$$\text{Plateau II}: \ 2Al_2Sr \leftrightarrow Al_4Sr + Sr\,(II) + 2e^- \tag{9}$$

$$\text{Plateau III}: \ Al_4Sr \leftrightarrow 4Al + Sr\,(II) + 2e^- \tag{10}$$

Using Eq. (6), the depolarization value of Sr on an Al electrode was calculated to be ~0.485 V.

3.3. Electrolysis and characterization of electrolysis products

From the results obtained, we observed that the depolarizing effect of Sr on both Zn and Al electrodes was stronger than that of Li, with specific depolarization values shown in Fig. 9. The figure shows the equilibrium potentials of redox

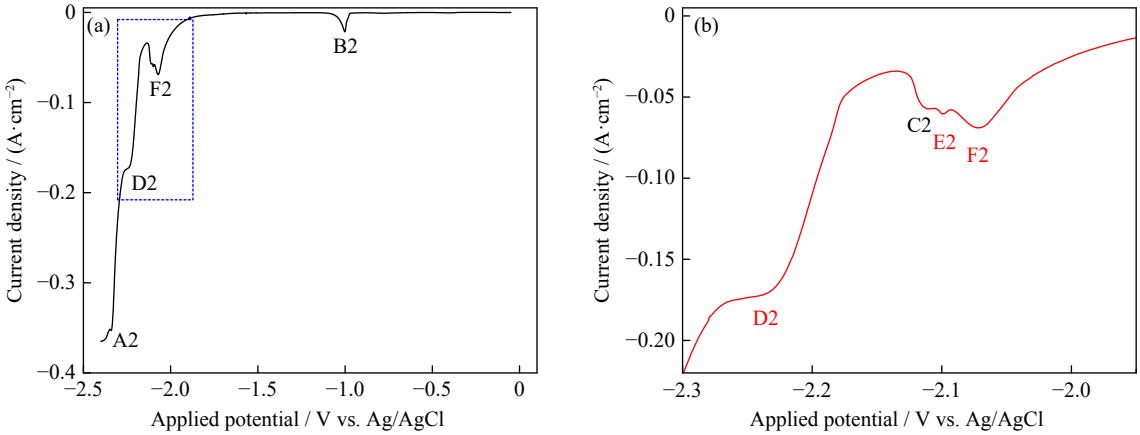

Fig. 6. (a) SWV curve obtained in LiCl–KCl–$AlCl_3$ (0.5wt%)–$SrCl_2$ (3wt%) molten salt on a W electrode (S = 0.322 cm^2); (b) the corresponding magnified curve.

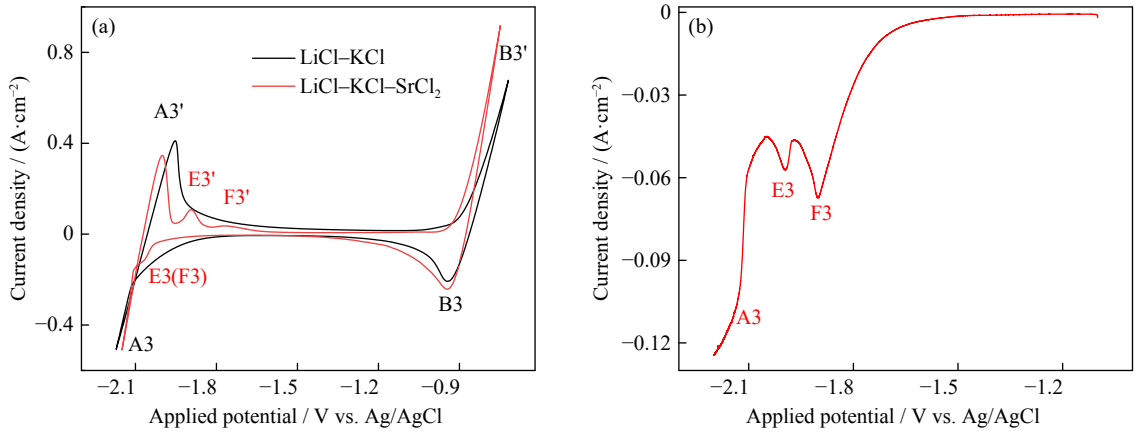

Fig. 7. (a) CV curves and (b) SWV obtained for LiCl–KCl–$SrCl_2$ (3wt%) molten salt on an Al electrode (S = 0.322 cm^2).

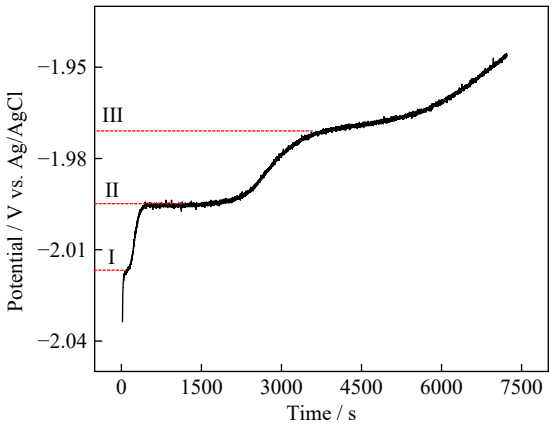

Fig. 8. OCP curve recorded for LiCl–KCl–$SrCl_2$ (3wt%) molten salt. Working electrode: Al; electrode area: 0.408 cm^2; deposition potential: −2.15 V; deposition time: 20 s.

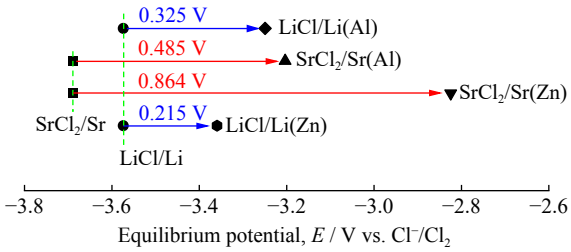

Fig. 9. Equilibrium potentials of redox couples on Al and Zn electrodes compared with standard electrode potential at 773 K.

couples on the Zn and Al electrodes compared with the standard electrode potential at 773 K. The line between the two equilibrium potentials of each species represents the shift in electrode potential. Clearly, the equilibrium potentials of the alloys (Al–Li, Al–Sr, Zn–Li, Zn–Sr) deviate from the standard potentials, which depend on the decreased thermodynamic activities of Sr and Li on the Al/Zn electrode. In addition, compared with Li, Sr has a more pronounced depolarization effect on the Al/Zn active electrode. Consequently, theoretically, Sr can be extracted while mitigating the codeposition of Li.

On the basis of the feasibility of extracting Sr in Zn, GITT was employed with 2 g of Zn as the working electrode, extracting Sr from the LiCl–KCl–$SrCl_2$ (3wt%) molten salt. Fig. 10 shows the curve obtained via deposition at a constant current of −1 mA for 500 s, then disconnecting the circuit and equilibrating for 200 s, repeated 200 times. The black curve represents the constant potential electrolysis curve, and the red curve represents the OCP curve. The equilibrium potential reaches a turning point when the cycle number reaches 45, indicating that the saturation solubility of Sr in Zn has been reached, following which the formation of Zn–Sr intermetallic compounds begins. The electrode potential of Sr in Zn ceases to change even upon continued electrolysis. The inserted image is a sample of the product.

During the electrolysis process, molten salt samples were taken at various time points for inductively coupled plasma (ICP) testing, allowing for the calculation of changes in Sr concentration and current efficiency throughout the process. From Fig. 11, one can see that the maximum current efficiency during the electrolysis was 53.93%, which gradually decreased with diminishing Sr concentration in the molten salt system. The low current efficiency is primarily attributed to some of the Sr extracted into Zn reacting with LiCl to convert again to $SrCl_2$ [20]. As per the ICP results, the solubility of Sr in Zn is ~0.276wt% at 773 K.

The alloy samples shown in Fig. 10 were bisected, and the cut surfaces were subsequently polished using various grades of SiC sandpaper, followed by a polishing process. The treated samples were analyzed via backscattered electron

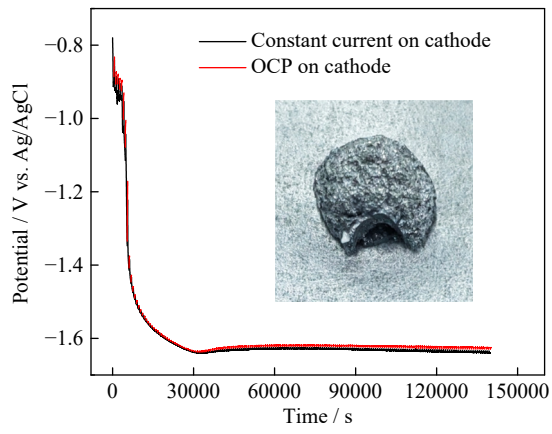

Fig. 10. Evolution of GITT electrolysis curve on liquid Zn electrode in LiCl–KCl–$SrCl_2$ (3wt%) at 773 K. Inserted image: sample of the product.

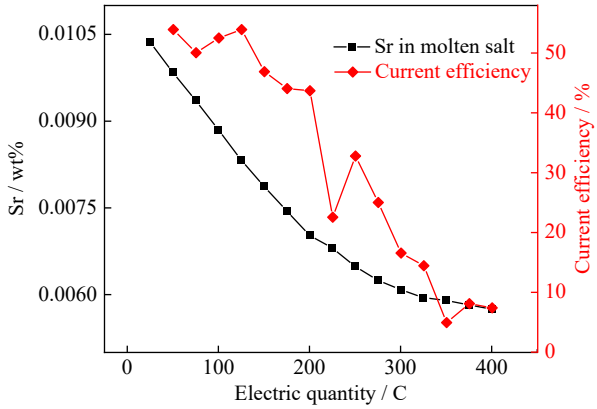

Fig. 11. Sr concentration in the molten salt (black curve) and current efficiency (red curve) during the electrolysis process.

SEM, as shown in Fig. 12(a–c), allowing for distinct identification of pure Zn and Zn–Sr alloy regions. Sr gradually deposited into Zn, and Zn–Sr intermetallic compounds began to form upon reaching saturation. Fig. 12(d) shows a line scan analysis indicated by the red arrow in Fig. 12(a). The absorption intensity of Zn remained almost unchanged, indicating a relatively uniform distribution of Zn on the surface, whereas the variation in absorption intensity of Sr was associated with the distribution of the Zn–Sr alloy.

By conducting XRD analysis of the electrolysis products, the composition of the Zn–Sr alloy was identified as the intermetallic compound $Zn_{13}Sr$, as shown in Fig. 13.

Sr was extracted via electrolysis using an Al electrode at a constant current of −15 mA for 2 h in LiCl–KCl–$SrCl_2$ (3wt%) molten salt. Fig. 14 shows the SEM–EDS analysis results of the product. Contrary to the extraction of Sr in liquid Zn, the distribution of Al post extraction exhibited inhomogeneity, as shown in Fig. 14(b). This was because Al

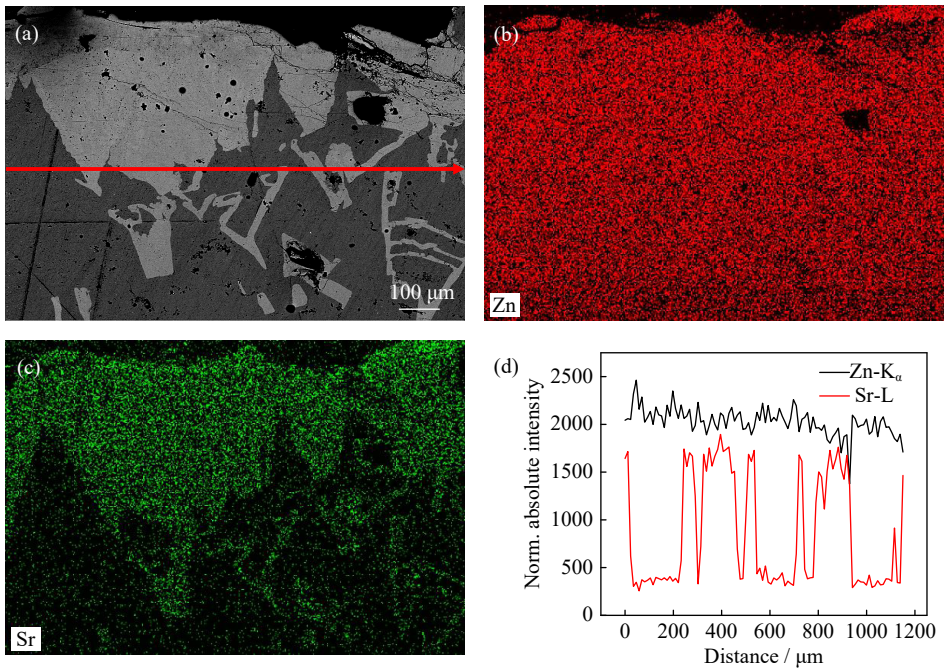

Fig. 12. (a) Backscattered electron SEM image of Zn–Sr alloy; (b, c) EDS elemental mapping of Zn–Sr alloy; (d) absolute intensity for Zn and Sr of red arrow area in (a).

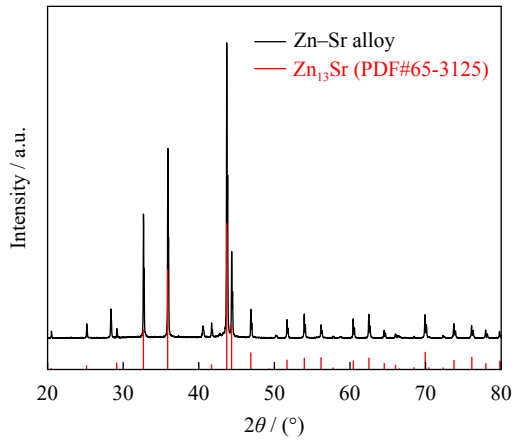

Fig. 13. XRD analysis results of the sample in Fig. 12.

was the excess phase in the sample, and the extracted Sr did not form intermetallic compounds with all the Al. In addition, the atomic ratios of $Zn_{13}Sr$ and Al_4Sr were 13:1 and 4:1, respectively. Consequently, the atomic density of Zn per unit area was higher, which resulted in the appearance of a more uniform distribution of Zn (Fig. 12(b)), whereas Al appeared unevenly distributed (Fig. 14(b)).

Next, we performed an XRD analysis of the sample shown in Fig. 14, revealing the formation of the intermetallic compound Al_4Sr (Fig. 15). Of the three intermetallic compounds in the Al–Sr system, Al_4Sr represented the Al-rich phase and was experimentally confirmed to be a stable intermetallic compound.

3.4. Calculated formation energy of the Zn–Sr and Al–Sr intermetallic compounds

We next examined the Zn–Sr and Al–Sr binary alloy phase diagrams [32–33]. Although both Zn–Sr and Al–Sr

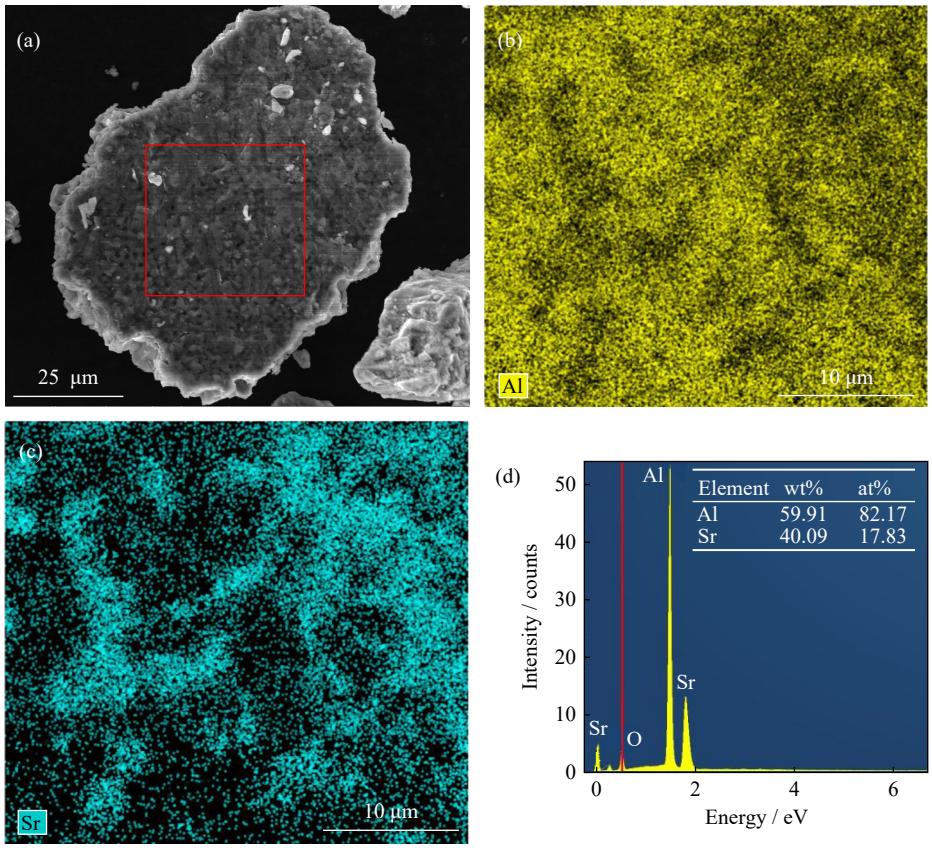

Fig. 14. (a) SEM image of Al–Sr alloy; (b–d) EDS elemental mappings of Al–Sr alloy.

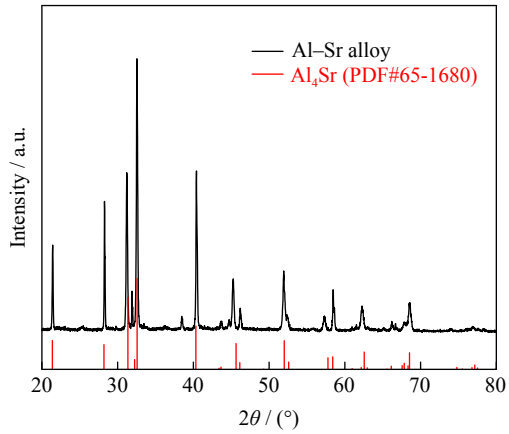

Fig. 15. XRD analysis results of the sample in Fig. 14.

systems contain various intermetallic compounds, in this study, the products extracted on the Al and Zn electrodes were uniquely identified as Al_4Sr and $Zn_{13}Sr$, respectively. Therefore, we investigated the stability of Zn–Sr and Al–Sr intermetallic compounds across a broad stoichiometry range by calculating their formation energies. The formation energies of all experimentally obtained Zn–Sr and Al–Sr intermetallic compounds were determined via computational means.

Fig. 16(a) shows the calculated formation energies of various Zn–Sr intermetallic compounds, with the cubic phases of Zn and Sr selected as the reference states. The calculation results of the convex hulls demonstrated that among the Zn–Sr structures studied, all Zn–Sr intermetallic compounds

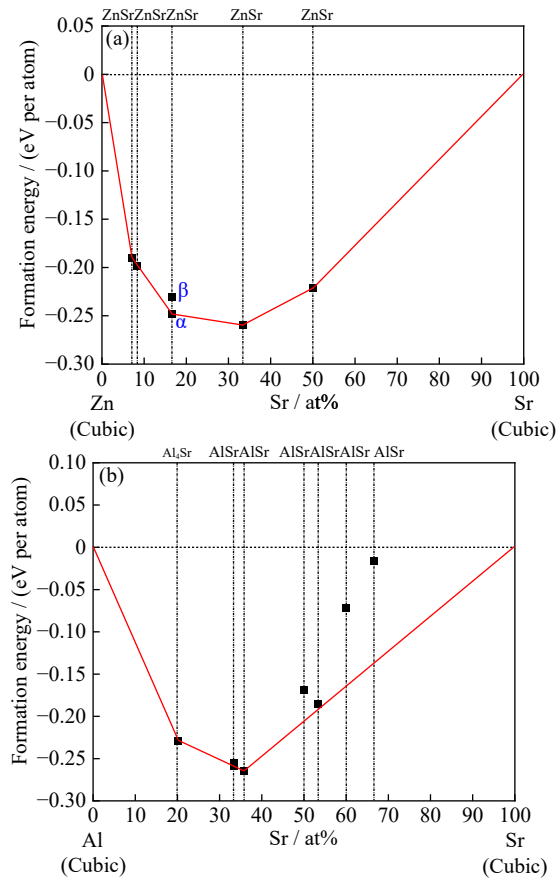

Fig. 16. Calculated formation energy of various (a) Zn–Sr and (b) Al–Sr intermetallic compounds as based on experimental observation.

were of stable phases except the hexagonal phase β-Zn_5Sr. Of these, Zn_2Sr was identified as the most stable compound against all studied Zn–Sr intermetallic compounds. However, in this study, the electrolytic product was solely $Zn_{13}Sr$, which is likely primarily associated with the kinetics of nucleation and growth within the Zn–Sr system.

Similarly, the cubic phases of Al and Sr were selected as the reference phase. Calculations were performed for all Al–Sr intermetallic compounds experimentally obtained, as shown in Fig. 16(b). The calculated convex hulls indicate that among the studied Al–Sr structures, Al_4Sr, Al_2Sr, and Al_9Sr_5 are stable intermetallic compounds. Of these, Al_9Sr_5 is the most stable one, and the orthorhombic phase of Al_2Sr is not a stable phase. Integration of the experimental results and theoretical calculations for both Zn–Sr and Al–Sr systems demonstrated that the electrolysis products were stable intermetallic compounds. However, this highlights that the formed intermetallic compounds may not necessarily be thermodynamically the most stable phases, which is also associated with kinetic nucleation and growth. Furthermore, the compounds of Zn–Sr and Al–Sr analyzed in Fig. 16 are more in number than those reported in their respective binary phase diagrams, thereby supplementing the associated parameters of the phase diagrams.

4. Conclusions

This study primarily explored interactions between Sr and reactive Zn/Al electrodes, confirming the feasibility of extraction and separation of Sr accumulated in electrorefining molten salts. Zn and Al demonstrated potential as electrode materials for extraction of Sr from molten salts post electrorefining. The enhanced chemical interaction between Zn and Sr, along with the liquid state of Zn under the experimental conditions, suggested superior extraction and separation efficiencies in practical applications.

(1) The codeposition behavior of Sr(II) with Zn(II)/Al(III) on inert electrodes in LiCl–KCl molten salt at 773 K was investigated using electrochemical techniques, namely CV, SWV, OCP, and CP. The diffusion coefficient of Zn in molten salt was calculated to be 1.65×10^{-5} $cm^2 \cdot s^{-1}$, and that of Sr on the Zn film electrode was determined to be 6.71×10^{-6} $cm^2 \cdot s^{-1}$. The polarization values of Sr on the Zn and Al electrodes were 0.864 and 0.485 V, respectively, indicating a stronger chemical interaction between Sr and Zn than that between Sr and Al. The ICP analysis results revealed the solubility of Sr in Zn at 773 K to be ~0.276wt%.

(2) Sr was extracted by forming alloys with Zn and Al via GITT and constant potential electrolysis, respectively. For LiCl–KCl molten salt containing 3wt% $SrCl_2$, the ICP results indicated that the maximum coulombic efficiency of Sr extracted on the reactive Zn electrode was ~54%. $Zn_{13}Sr$ and Al_4Sr were identified via XRD and SEM–EDS, with no codeposition of Li observed. Through DFT calculation results, the deposited products $Zn_{13}Sr$ and Al_4Sr were observed to be stable phases of the respective intermetallic compounds.

Acknowledgements

This work was financially supported by the National Postdoctoral Program for Innovative Talents, China (No. BX2021327), the National Natural Science Foundation of China (Nos. 22206194 and U2267222), the Ningbo Natural Science Foundation of China (No. 2023J337), and the Yongjiang Talent Introduction Programme, China (No. 2021A-161-G).

Conflict of Interest

The authors declare that they have no known competing financial interests or personal relationships that could have appeared to influence the work reported in this paper.

References

[1] A.Y. Galashev, Recovery of actinides and fission products from spent nuclear fuel via electrolytic reduction: Thematic overview, *Int. J. Energy Res.*, 46(2022), No. 4, p. 3891.

[2] P. Baron, S.M. Cornet, E.D. Collins, *et al*., A review of separation processes proposed for advanced fuel cycles based on technology readiness level assessments, *Prog. Nucl. Energy*, 117(2019), art. No. 103091.

[3] B.J. Riley, Electrochemical salt wasteform development: A review of salt treatment and immobilization options, *Ind. Eng. Chem. Res.*, 59(2020), No. 21, p. 9760.

[4] G.L. Fredrickson, M.N. Patterson, D. Vaden, *et al*., History and status of spent fuel treatment at the INL Fuel Conditioning Facility, *Prog. Nucl. Energy*, 143(2022), art. No. 104037.

[5] J.H. Choi, T.K. Lee, K.R. Lee, *et al*., Melt-crystallization monitoring system for the purification of 10 kg-scale LiCl salt waste, *Nucl. Eng. Des.*, 326(2018), p. 1.

[6] M.F. Simpson, Projected salt waste production from a commercial pyroprocessing facility, *Sci. Technol. Nucl. Install.*, 2013(2013), art. No. 945858.

[7] H.C. Eun, Y.Z. Cho, S.M. Son, *et al*., Recycling of LiCl–KCl eutectic based salt wastes containing radioactive rare earth oxychlorides or oxides, *J. Nucl. Mater.*, 420(2012), No. 1-3, p. 548.

[8] T.S. Yoo, S.M. Frank, M.F. Simpson, P.A. Hahn, T.J. Battisti, and S. Phongikaroon, Salt-zeolite ion-exchange equilibrium studies for a complete set of fission products in molten LiCl–KCl, *Nucl. Technol.*, 171(2010), No. 3, p. 306.

[9] M. Shaltry, S. Phongikaroon, and M.F. Simpson, Ion exchange kinetics of fission products between molten salt and zeolite-A, *Microporous Mesoporous Mater.*, 152(2012), p. 185.

[10] H.C. Eun, Y.Z. Cho, H.S. Park, I.T. Kim, and H.S. Lee, Study on a separation method of radionuclides (Ba, Sr) from LiCl salt wastes generated from the electroreduction process of spent nuclear fuel, *J. Radioanal. Nucl. Chem.*, 292(2012), No. 2, p. 531.

[11] V.A. Volkovich, T.R. Griffiths, and R.C. Thied, Treatment of molten salt wastes by phosphate precipitation: Removal of fission product elements after pyrochemical reprocessing of spent nuclear fuels in chloride melts, *J. Nucl. Mater.*, 323(2003), No. 1, p. 49.

[12] I. Amamoto, H. Kofuji, M. Myochin, Y. Takasaki, T. Yano, and T. Terai, Precipitation behaviors of fission products by phosphate conversion in LiCl–KCl medium, *Nucl. Technol.*, 171(2010), No. 3, p. 316.

[13] Y.Z. Cho, T.K. Lee, H.C. Eun, J.H. Choi, I.T. Kim, and G.I. Park, Purification of used eutectic (LiCl–KCl) salt electrolyte

from pyroprocessing, *J. Nucl. Mater.*, 437(2013), No. 1-3, p. 47.
[14] H.S. Lee, G.H. Oh, Y.S. Lee, I.T. Kim, E.H. Kim, and J.H. Lee, Concentrations of CsCl and $SrCl_2$ from a simulated LiCl salt waste generated by pyroprocessing by using czochralski method, *J. Nucl. Sci. Technol.*, 46(2009), No. 4, p. 392.
[15] Y.Z. Cho, G.H. Park, H.S. Lee, I.T. Kim, and D.S. Han, Concentration of cesium and strontium elements involved in a LiCl waste salt by a melt crystallization process, *Nucl. Technol.*, 171(2010), No. 3, p. 325.
[16] A.N. Williams, S. Phongikaroon, and M.F. Simpson, Separation of CsCl from a ternary CsCl–LiCl–KCl salt *via* a melt crystallization technique for pyroprocessing waste minimization, *Chem. Eng. Sci.*, 89(2013), p. 258.
[17] M. Matsumiya, R. Takagi, and R. Fujita, Recovery of Eu^{2+} and Sr^{2+} using liquid metallic cathodes in molten NaCl–KCl and KCl system, *J. Nucl. Sci. Technol.*, 34(1997), No. 3, p. 310.
[18] Y.H. Liu, M. Tang, S. Zhang, *et al*., U(VI) adsorption behavior onto polypyrrole coated 3R-MoS_2 nanosheets prepared with the molten salt electrolysis method, *Int. J. Miner. Metall. Mater.*, 29(2022), No. 3, p. 479.
[19] S.S. Liu, S.L. Li, C.H. Liu, J.L. He, and J.X. Song, Effect of fluoride ions on coordination structure of titanium in molten NaCl–KCl, *Int. J. Miner. Metall. Mater.*, 30(2023), No. 5, p. 868.
[20] S.W. Kim, M.K. Jeon, and E.Y. Choi, Electrolytic behavior of $SrCl_2$ and $BaCl_2$ in LiCl molten salt during oxide reduction in pyroprocessing, *J. Radioanal. Nucl. Chem.*, 321(2019), No. 1, p. 361.
[21] T. Lichtenstein, T.P. Nigl, N.D. Smith, and H. Kim, Electrochemical deposition of alkaline-earth elements (Sr and Ba) from LiCl–KCl–$SrCl_2$–$BaCl_2$ solution using a liquid bismuth electrode, *Electrochim. Acta*, 281(2018), p. 810.
[22] T. Lichtenstein, T.P. Nigl, and H. Kim, Recovery of alkaline-earths into liquid Bi in ternary LiCl–KCl–$SrCl_2$/$BaCl_2$ electrolytes at 500°C, *J. Electrochem. Soc.*, 167(2020), No. 10, art. No. 102501.
[23] T.P. Nigl, T. Lichtenstein, Y.R. Kong, and H. Kim, Electrochemical separation of alkaline-earth elements from molten salts using liquid metal electrodes, *ACS Sustainable Chem. Eng.*, 8(2020), No. 39, p. 14818.
[24] M.E. Woods and S. Phongikaroon, Assessment on recovery of cesium, strontium, and barium from eutectic LiCl–KCl salt with liquid bismuth system, *J. Nucl. Fuel Cycle Waste Technol.*, 18(2020), No. 4, p. 421.
[25] J. Jang, M. Lee, G.Y. Kim, and S.C. Jeon, Cesium and strontium recovery from LiCl–KCl eutectic salt using electrolysis with liquid cathode, *Nucl. Eng. Technol.*, 54(2022), No. 10, p. 3957.
[26] I. Barin and G. Platzki, *Thermochemical Data of Pure Substances*, Weinheim, New York, 1989, p. 30.
[27] P.E. Blöchl, Projector augmented-wave method, *Phys. Rev. B*, 50(1994), No. 24, p. 17953.
[28] G. Kresse and J. Furthmüller, Efficient iterative schemes for ab initio total-energy calculations using a plane-wave basis set, *Phys. Rev. B*, 54(1996), No. 16, p. 11169.
[29] Y.L. Liu, L.Y. Yuan, K. Liu, *et al*., Electrochemical extraction of samarium from LiCl–KCl melt by forming Sm–Zn alloys, *Electrochim. Acta*, 120(2014), p. 369.
[30] T.Q. Yin, L. Chen, Y. Xue, *et al*., Electrochemical behavior and underpotential deposition of Sm on reactive electrodes (Al, Ni, Cu and Zn) in a LiCl–KCl melt, *Int. J. Miner. Metall. Mater.*, 27(2020), No. 12, p. 1657.
[31] A.J. Bard and L.R. Faulkner, *Electrochemical Methods*: *Fundamentals and Applications*, Wiley, New York, 1980, p. 801.
[32] C. Wang, Z.P. Jin, and Y. Du, Thermodynamic modeling of the Al–Sr system, *J. Alloys Compd.*, 358(2003), No. 1-2, p. 288.
[33] P.J. Spencer, A.D. Pelton, Y.B. Kang, P. Chartrand, and C.D. Fuerst, Thermodynamic assessment of the Ca–Zn, Sr–Zn, Y–Zn and Ce–Zn systems, *Calphad*, 32(2008), No. 2, p. 423.